

A hadronic emission model for black hole-disc impacts in the blazar OJ 287

J. C. Rodríguez-Ramírez,^{1*} P. Kushwaha,^{1,2†} E. M. de Gouveia Dal Pino^{1‡} and R. Santos-Lima^{1§}

¹*Instituto de Astronomia, Geofísica e Ciências Atmosféricas (IAG-USP), Universidade de São Paulo. São Paulo-SP 05508-090, Brasil.*

²*Aryabhata Research Institute of Observational Sciences (ARIES). Nainital 263002, India.*

Accepted 2020 August 26. Received 2020 August 23; in original form 2020 May 1.

ABSTRACT

A super-massive black hole (SMBH) binary in the core of the blazar OJ 287 has been invoked in previous works to explain its observed optical flare quasi-periodicity. Following this picture, we investigate a hadronic origin for the X-ray and γ -ray counterparts of the November 2015 major optical flare of this source. An impact outflow must result after the lighter SMBH (the secondary) crosses the accretion disc of the heavier one (the primary). We then consider acceleration of cosmic-ray (CR) protons in the shock driven by the impact outflow as it expands and collides with the active galactic nucleus (AGN) wind of the primary SMBH. We show that the emission of these CRs can reproduce the X-ray and γ -ray flare data self-consistently with the optical component of the November 2015 major flare. The derived emission models are consistent with a magnetic field $B \sim 5$ G in the emission region and a power-law index of $q \sim 2.2$ for the energy distribution of the emitting CRs. The mechanical luminosity of the AGN wind represents $\lesssim 50\%$ of the mass accretion power of the primary SMBH in all the derived emission profiles.

Key words: accretion – shock waves – astroparticle physics – radiation mechanisms: non-thermal

1 INTRODUCTION

Theoretical arguments as well as indirect observational evidence suggest the presence of super-massive black hole (SMBH) pairs coalescing in the core of certain galaxies. Galaxy mergers (Springel et al. 2005), for instance, might be a natural process leading to the formation of such SMBH binaries. Compelling examples of active galactic nuclei (AGNs) approaching each other can be found in the recent works by, e. g., Pfeifle et al. (2019) and Deane et al. (2014), where the SMBHs of approaching AGNs are localised at distances from tens to hundreds of parsecs between each other.

When the distance among two SMBHs shrinks to sub-parsec scales, the system is theoretically expected to enter its gravitational wave (GW)-driven regime for orbital decay. In such a stage, SMBH binaries are thought to be the most prominent sources of GWs in the cosmos (Begelman et al. 1980; Mingarelli et al. 2017). Current instruments however,

are not able to detect either GWs from SMBHs systems (expected in the nHz- μ Hz domain), or resolve SMBHs binaries at sub-parsec scales. Alternatively, indirect signatures as double line emission (Popović 2012) and quasi-periodical flares in certain AGNs (Komossa & Zensus 2016) are employed to trace the presence of compact, orbiting SMBH pairs. Due to a persistent quasi-periodical feature in optical, the blazar OJ 287 is perhaps the strongest candidate for hosting a sub-parsec SMBH pair (Dey et al. 2018).

OJ 287 (at a red-shift $z = 0.306$) is categorised as a BL Lac object and is known for its regular ~ 12 year, double peaked optical variations registered for over 130 years (Sillanpaa et al. 1988; Hudec et al. 2013). These periodic features have motivated a number of possible explanations (e.g., Lehto & Valtonen 1996; Katz 1997; Tanaka 2013; Britzen et al. 2018). Particularly, the SMBH binary scenario proposed by Lehto & Valtonen (1996) (see also Valtonen et al. 2008) appears to predict naturally the timing of the double peaked observed outbursts. Additionally, this model is consistent with the sharp rise of the flare emission and its low polarisation degree, being these aspects not satisfactorily explained by other models (see Dey et al. 2019; Kushwaha 2020, for more details).

* E-mail: juan.rodriguez@iag.usp.br

† E-mail: pankaj.tifr@gmail.com

‡ E-mail: dalpino@iag.usp.br

§ E-mail: lima.reinaldo.santos.de@gmail.com

The SMBH binary model of [Lehto & Valtonen \(1996\)](#) explains the periodical outbursts of OJ 287 in terms of thermal bremsstrahlung radiation of the outflows generated by the impacts of the lighter SMBH (the secondary) on the accretion disc of the heavier one (the primary, see also [Pihajoki 2016](#)). Within this picture, a general relativistic (GR) approach for the orbit of the secondary BH predicted the starting times of the 1994, 1995, 2005, 2007, and 2015 flares ([Valtonen et al. 2008, 2016](#)). With the observed data from the last three outbursts, the BH masses of the the binary have been constrained to $M_1 = 1.83 \times 10^{10} M_\odot$ and $M_2 = 1.5 \times 10^8 M_\odot$ for the primary and secondary BHs, respectively ([Valtonen et al. 2016](#)).

While the analysis developed in, [Lehto & Valtonen \(1996\)](#), [Ivanov et al. \(1998\)](#), and [Pihajoki \(2016\)](#) is applicable to the problem of a BH threading quasi-perpendicularly an accretion disc, other studies in the context of star-disc collisions (and their observational consequences) can be found in, e. g., [Zentsova \(1983\)](#), [Nayakshin et al. \(2004\)](#), and [Kieffer & Bogdanović \(2016\)](#).

As expected from BL Lac objects, OJ 287 displays X-ray as well as γ -ray flaring behaviour ([Neronov & Vovk 2011](#); [Hodgson et al. 2017](#); [Kushwaha et al. 2013, 2018b,c](#); [Pal et al. 2020](#)). Particularly, [Kushwaha et al. \(2018b\)](#) analyse the multi-wavelength (MW) light curves (LCs) of OJ 287 during and after the November 2015 major optical flare. These authors extracted the corresponding spectral energy distribution (SED) of the flare and interpreted it with a leptonic, jet emission model. They found that the X-ray component of the flare is well explained by synchrotron self-Compton (SSC) emission, whereas the γ -ray flare component is better explained with external Compton (EC) emission (see also [Kushwaha et al. 2018a](#)).

In the present paper we consider the observed MW SED obtained by [Kushwaha et al. \(2018b\)](#) and alternatively investigate a hadronic origin for the high energy (HE) counterpart (the simultaneous X-ray and γ -ray excess) of the November 2015 optical flare. We follow the SMBH-disc impact model of [Lehto & Valtonen \(1996\)](#) (see also [Pihajoki 2016](#)) and explain the X-ray and γ -ray fluxes with emission triggered by proton-proton (p - p) interactions of cosmic-rays (CRs) with the thermal ions within the impact outflow. In the scenario proposed here, we consider CR shock acceleration driven by the collision of the outflow and the AGN wind of the primary SMBH, as depicted in Figure 1.

This paper is organised as follows. In the next section, we characterise the SMBH-disc impact outflow and its thermal radiation following the considerations of previous works. In Section 3, we describe the non-thermal radiation that results due to p - p interactions of CRs with the thermal ions of the outflow. In Section 4, we apply the non-thermal emission model to explain the MW SED corresponding to the 2015 major flare of OJ 287. We finally summarise and discuss our results in Section 5.

2 THE OUTFLOW FROM THE SMBH-DISC IMPACT

2.1 The outflow thermal flare

After the secondary SMBH threads the accretion disc of the primary, two outflows emerge, one above and the other below

the accretion disc at the location of the impact. This effect was simulated by [Ivanov et al. \(1998\)](#) with a hydrodynamical approach. Following [Ivanov et al. \(1998\)](#) and [Pihajoki \(2016\)](#), here we assume a BH-disc impact event that produces a bipolar outflow. Additionally, we consider that only the outflow emerging in the side of the disc pointing toward us contributes to the observed outburst SED. The analysis described in the following is centred on this “observer side” outflow which we model as a spherical expanding bubble. A cartoon of this outflow is depicted in Figure 1a. Within this picture, after the BH-disc impact occurs, a bubble emerges from the disc with an initial radius R_0 , gas density ρ_0 , and temperature T_0 .

Here we parametrise the initial radius of the bubble as a fraction f_R of the the Bondi-Hoyle-Lyttleton radius R_{HL} ([Hoyle & Lyttleton 1939](#); [Edgar 2004](#)) of the secondary SMBH of mass M_2 , i.e:

$$R_0 = f_R R_{\text{HL}}; f_R \leq 1, \quad (1)$$

with

$$R_{\text{HL}} = \frac{2GM_2}{v_r^2}, \quad (2)$$

where v_r is the velocity of the disc material in the co-moving frame of the travelling BH at the impact event¹. Following [Lehto & Valtonen \(1996\)](#), we estimate the initial temperature and density of the outflow bubble with the jump conditions for a strong, radiation dominated shock ([Pai & Luo 1991](#); where this shock is driven by the secondary BH during its passage through the accretion disc, see Appendix A):

$$T_0 = \left(\frac{18\rho_d v_r^2}{7a} \right)^{1/4}, \quad (3)$$

$$\rho_0 = \left(\frac{\gamma_a + 1}{\gamma_a - 1} \right) \rho_d = 7\rho_d. \quad (4)$$

In equations (3)-(4) ρ_d is the gas density of the disc at the location of the impact, a is the radiation constant, and $\gamma_a = 4/3$ is the adiabatic index appropriate for a radiation-dominated mixture. The initial energy of the emerging outflow can be estimated as (see Appendix A for details):

$$E_0 = \frac{14\pi}{3} (f_R R_{\text{HL}})^3 \rho_d v_r^2 = 8.3 \times 10^{55} \times \left(\frac{M_2}{1.5 \times 10^8 M_\odot} \right)^3 \left(\frac{f_R}{0.6} \right)^3 \left(\frac{n_d}{10^{14} \text{ cm}^{-3}} \right) \left(\frac{0.15c}{v_r} \right)^4 \text{ erg}, \quad (5)$$

where the quantities in the second equality are normalised with typical values for the parameters of the claimed binary system in OJ 287 ([Valtonen et al. 2019](#)).

In an adiabatic expansion, when the bubble attains a radius $R_b > R_0$ its temperature T_b and gas density ρ_b are:

$$T_b = T_0 \xi^{3(1-\gamma_a)}, \quad (6)$$

$$\rho_b = \rho_0 \xi^{-3}, \quad (7)$$

where $\xi \equiv R_b / R_0$.

¹ Considering the toroidal component of the disc velocity \vec{v}_ϕ and the velocity of the secondary SMBH \vec{v}_{orb} at the location of the impact, the velocity of the disc material in the co-moving frame of the secondary BH is $v_r \sim |\vec{v}_{\text{orb}} - \vec{v}_\phi|$ (see Appendix A).

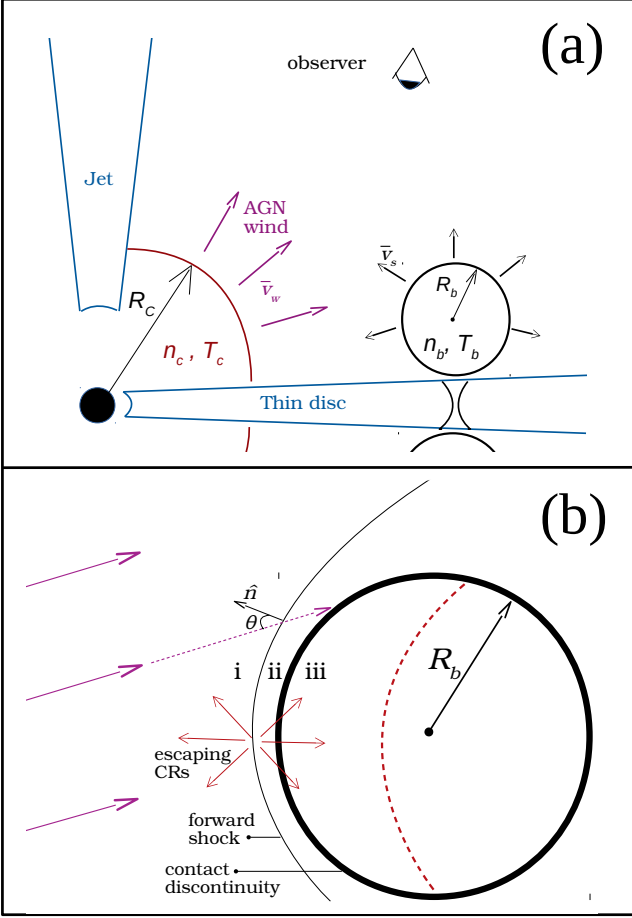


Figure 1. (a) Schematic illustration of an idealised spherical outflow that expands above the accretion disc of the primary SMBH. The outflow is thought to be generated by a previous impact of the secondary SMBH on the accretion disc of the primary (see the text). In the scenario proposed here, the impact outflow forms a shock due to its interaction with the AGN wind driven by the primary SMBH, whose poloidal components are represented with the purple arrows. (b) Amplified view of the spherical outflow of the upper panel. The thick solid circle represents the boundary of the outflow material and the thin solid curve is the driven shock. The dashed red curve represents the boundary of the CR emission volume proposed in this work (see the text). The regions of this schematic figure are: (i) the unperturbed AGN wind of density n_w , (ii) the swept up shell of the shocked wind material, and (iii) the CR emission volume within the outflow bubble of density n_b .

Similarly to [Lehto & Valtonen \(1996\)](#) (see also [Valtonen et al. 2019](#)), we consider that the optical outburst is produced after the spherical bubble expands adiabatically and the effective optical depth τ_e meets the transparency condition:

$$\tau_e = \sqrt{\kappa_a \kappa_T} \rho_b R_b = 1. \quad (8)$$

In equation (8), κ_T is the electron opacity and κ_a is the frequency-averaged opacity due to absorption. For a fully ionised gas $\kappa_T = \sigma_T / (\mu_e m_u)$ where σ_T is the electron scattering cross section, m_u is the atomic mass constant, $\mu_e = 2/(1+X)$, and X the hydrogen mass fraction. According to [Lehto & Valtonen \(1996\)](#) (see also [Valtonen et al.](#)

2019), the absorption opacity κ_a within the outflow bubble follows Kramer’s law with contributions due to free-free and bound-free opacities derived from Rosseland mean. In this approach, the absorption opacity can be written as:

$$\kappa_a = K_a \rho_b T_b^{-7/2} \text{ cm}^2 \text{ g}^{-1}, \quad (9)$$

with

$$K_a = 3.7 \times 10^{22} (1+X) \left[1 + \left(\frac{1180}{t_{bf}} - 1 \right) Z \right], \quad (10)$$

where X and Z are the mass fractions of hydrogen and metals, respectively, and t_{bf} is known as the guillotine factor (correction for quantum effects of bound-free transitions) which takes values between 100 and 1 ([Irwin 2007](#)).

Condition (8) together with equations (6)-(7) and (9)-(10) define the radius of the expanding outflow at which the thermal flare is produced:

$$\frac{R_b}{R_0} \equiv \xi = \left(K_a \kappa_T R_0^2 \rho_0^3 T_0^{-7/2} \right)^{2/7}, \quad (11)$$

which is determined by the initial radius R_0 , density ρ_0 , and temperature T_0 of the outflow.

Given the values of v_r , ρ_d , and f_R , one can determine the properties of the outflow bubble when it produce the outburst. First, R_0 , ρ_0 , and T_0 are obtained with equations (1)-(4), and then R_b , T_b , and ρ_b through equations (11), (6), and (7). The appropriate combination of the parameters v_r , ρ_d , and f_R can be constrained by fitting the implied thermal bremsstrahlung emission of the bubble of radius R_b , density ρ_b , and temperature T_b to the observed SED data of the optical flare (see Section 4). To do this, we calculate the observed flux due to thermal bremsstrahlung radiation as

$$\nu F_\nu = \nu' \pi \left(\frac{R_b}{D_L} \right)^2 I_{\nu'}, \quad (12)$$

where $\nu' = (1+z)\nu$, $z = 0.306$ is the redshift of the blazar OJ 287, $D_L = 1602$ Mpc its luminosity distance, and $I_{\nu'}$ is the specific intensity (calculated for ν') of the thermal bremsstrahlung radiation at the outer boundary of the outflow, i.e. at $R = R_b$. The spectrum due to optically thin bremsstrahlung emission can be obtained using

$$I_\nu = (4/3) R_b j_\nu, \quad (13)$$

where j_ν is the thermal bremsstrahlung emission coefficient which here is taken as

$$4\pi j_\nu = 6.8 \times 10^{-38} n_b^2 T_b^{-1/2} \exp \left\{ -\frac{h\nu}{kT_b} \right\} \text{ erg s}^{-1} \text{ cm}^{-3} \text{ Hz}^{-1}. \quad (14)$$

The spectrum given by equation (13) is correct as long as the medium producing the radiation is optically thin. For the outflow bubble defined by condition (11), this turns out to be the case at optical frequencies. However, this is not the case for lower frequencies where the emission is attenuated by self-absorption. To account for this effect present at low frequencies, one can alternatively employ the specific intensity:

$$I_\nu = B_\nu (1 - \exp\{-\tau_\nu\}), \quad (15)$$

$$\tau_\nu = \int_0^{4R_b/3} j_\nu / B_\nu ds \approx (4/3) R_b j_\nu / B_\nu, \quad (16)$$

which is thermal bremsstrahlung emission with self-absorption given by Kirchhoff's law and the black-body spectral radiance of temperature T_b :

$$B_\nu = \frac{2h\nu^3}{c^2} \left(\exp \left\{ \frac{h\nu}{kT_b} \right\} - 1 \right)^{-1}. \quad (17)$$

We consider the photon field density n_{ph} generated by thermal bremsstrahlung, as the target photon field for inverse Compton scattering of secondary electrons within the outflow (this radiation process is discussed in Section 3.2). We calculate this target photon field density (number of photons per unit energy, per unit volume) as

$$n_{\text{ph}}(\epsilon, T_b) = \frac{4\pi I_\nu(R_b, T_b)}{ch\epsilon}, \quad (18)$$

where $\epsilon = h\nu$ is the energy of the thermal bremsstrahlung photons. We also employ the photon field density of equation (18) to calculate the attenuation of the γ -rays due to photon-photon annihilation, as described in the following subsection.

We note that in all the models considered in this paper, there is no substantial difference between self-absorbed (equation 15) and optically thin bremsstrahlung emission (equation 13) at optical energy bands. For the parameters considered here, the spectra of these two approaches start to diverge for energies $\lesssim kT_b$. An example that illustrates this is shown in Figure 2, where the orange, solid curve is calculated using equation (13) (optically thin bremsstrahlung) and the orange, dashed curve is obtained using equation (15) (bremsstrahlung with self-absorption). Whereas this discrepancy is not substantial to model the optical outburst data, the difference between the two approaches can be noticeable in the resulting X-ray spectrum of relativistic electrons Comptonising the bubble radiation field (this HE process is described in Section 3.2). Since an optically thin bremsstrahlung spectrum is not physically possible for photons at arbitrary low energies, in this work we adopt the thermal spectrum given by equation (15). The spectrum that results from this bremsstrahlung self-absorbed emission is compatible with the thermal spectrum of BH-disc impact outflows proposed by Pihajoki (2016).

The time that the spherical outflow takes to expand from the initial radius R_0 to the outburst radius R_b depends on the dynamics of the expansion. Here we follow the expansion dynamics proposed by Lehto & Valtonen (1996). In this approach, the outer boundary of the outflow expands with a velocity equivalent to the speed of sound of the bubble internal gas, which is radiation pressure dominated. With this assumption the velocity of the outflow's outer boundary is

$$c_s = c_{s0} (R/R_0)^{-1/2}, \quad (19)$$

the radius of the outflow evolves with time as

$$R(t) = R_0 \left(1 + \frac{3}{2} \frac{c_{s0}}{R_0} t \right)^{2/3}, \quad (20)$$

and the time that the bubble takes to attain the outburst radius R_b is

$$\Delta t_b = \frac{2}{3} \frac{R_0}{c_{s0}} \left(\xi^{3/2} - 1 \right). \quad (21)$$

In equations (19)-(21), $c_{s0} = \sqrt{8/7}v_r$ is the initial speed of sound of the gas within bubble and v_r is the velocity of

the accretion disc material in the co-moving frame of the secondary BH at the impact event (Lehto & Valtonen 1996; Pihajoki 2016).

In short, in this work we consider a BH-disc impact scenario in which (i) the impact produces two outflows, one above and the other below the accretion disc (as proposed by Ivanov et al. 1998 and Pihajoki 2016), (ii) we attribute the observed emission to the outflow emerging in the direction of the observer only, and (iii) this outflow expands as described in Lehto & Valtonen (1996), Dey et al. (2018), and Valtonen et al. (2019). Within this approach, we employ the condition (11) to define the state of the expanding spherical outflow (e.g., radius, gas density, temperature) from which we calculate optical, X-ray, and γ -ray emission to model the MW 2015 flare data (see Section 4).

This is an idealised and simplified emission scenario. As discussed by Pihajoki (2016), outflows driven by BH-disc impacts might be far from having uniform internal structure. In addition, the vertical stratification of the disc and the gravitational influence of the primary SMBH would lead to a non-spherical outflow morphology. Regarding the opacity of the impact outflow, Kramer's formula (9) for the opacity of free-free and bound-free transitions is a very crude approximation for the absorption opacity when compared to more accurate numerical computations for static stellar interiors (Iglesias & Rogers 1996; Ferguson et al. 2005). Furthermore, the impact outflow discussed here is not static and the expanding nature of the emitting plasma introduces effects (Shibata et al. 2014; Pihajoki 2016), not quantified in the present emission model.

Surprisingly, despite neglecting the aforementioned physical effects, the emitting volume proposed by (Lehto & Valtonen 1996) appears to explain several aspects of the observed recurrent optical flares, not successfully explained by alternative models (see the introduction and references therein). Particularly, to explain the origin of the 2015 major optical outburst, Valtonen et al. (2019) consider the BH masses $M_1 = 1.835 \times 10^{10} M_\odot$ and $M_2 = 1.5 \times 10^8 M_\odot$ for the primary and secondary BHs, respectively, an impact distance of $R_{\text{imp}} \sim 17500$ AU from the primary BH where $n_d \sim 1.75 \times 10^{14} \text{ cm}^{-3}$, $v_r \sim 0.12c$, and an outflow bubble with initial radius $R_0 \sim 47$ AU. They follow Lehto & Valtonen (1996) to define the transparency condition of the emitting bubble (see equation 11) assuming $X = 0.85$, $Z = 0.02$ for the mass fractions of hydrogen and metals. If one considers the above parameters and the guillotine factor $t_{\text{bf}} = 25$ for the absorption opacity (see equation 10), the flux that results due to optically thin, thermal bremsstrahlung radiation employing equations (12)-(14) matches well with the optical data of the 2015 flare as shown in the blue solid curve in Figure 2. This thermal flux corresponds to a bubble that expands a factor of $\xi \sim 31$ (and not $\xi \sim 18$ which is perhaps a typo in the text of Valtonen et al. 2019), and has a temperature $T_b \sim 3.4 \times 10^4$ K and gas number density $n_b \sim 4.1 \times 10^{10} \text{ cm}^{-3}$ when it let the radiation escape freely (using $\xi = 18$ the calculated flux, which is plotted by the grey curve in Figure 2, overshoots the data considerably).

In this paper we investigate whether a BH-disc impact is a viable scenario to explain the simultaneous spectral changes in the broadband SED of OJ 287. We then look for the conditions that allow the outflow bubble described in this Section to account simultaneously for the optical, X-

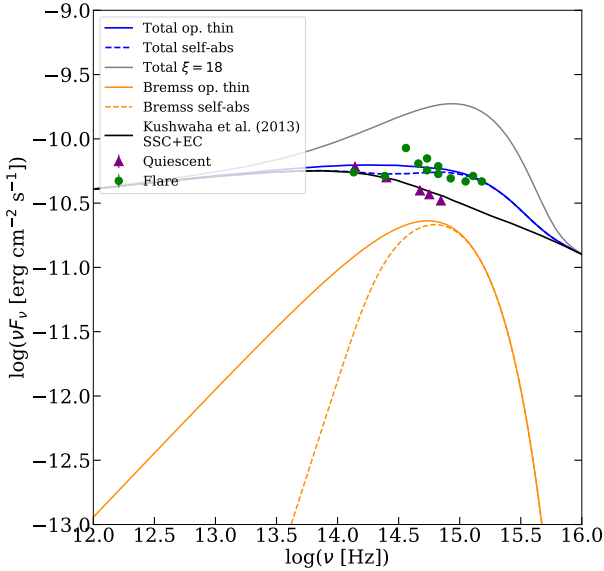


Figure 2. SED of the 2015 major flare (green data points) of OJ 287 at NIR-UV bands (adapted from Kushwaha et al. 2018b). The magenta data points correspond to a previous quiescent state and the black curve is a jet synchrotron emission model (both data and curve adapted from Kushwaha et al. 2013). See the text for the description of the different flare emission curves.

ray and γ -ray excess (we describe the HE emission model in Section 3). To do this, we use v_r , f_R and n_d as free parameters to obtain outflow bubbles with different properties (such as R_b , n_b , and T_b) which thermal emission is consistent with the optical data of the 2015 outburst. The masses of the SMBHs, primary $M_1 = 1.835 \times 10^{10} M_\odot$ and secondary $M_2 = 1.5 \times 10^8 M_\odot$ (taken from Dey et al. 2018), are considered fixed in this work. We also use the fixed values of $X = 0.85$ and $Z = 0.02$ for the mass fraction of hydrogen and metals (following Valtonen et al. 2019), and $t_{bf} = 5$ for the guillotine factor of absorption opacity within the outflow bubble. These values appear to be appropriate for the bubble models considered here and also provide a good agreement with the data.

2.2 The opacity of the impact outflow to gamma-ray photons

The flux of potential γ -rays produced in the impact outflow is susceptible to be attenuated by internal absorption. We consider the thermal bremsstrahlung radiation discussed in this Section as the dominant source of soft photons for γ -ray annihilation. If $L^0(E_\gamma)$ is the luminosity of γ -ray photons of energy E_γ produced in the impact outflow, the luminosity of γ -rays that escape the emission region can be calculated as $L(E_\gamma) = L^0(E_\gamma) \exp\{-\tau_{\gamma\gamma}(E_\gamma)\}$, where $\tau_{\gamma\gamma}$ is the optical depth of photon-photon annihilation.

To calculate $\tau_{\gamma\gamma}$ we assume for simplicity that the thermal bremsstrahlung photon field is isotropic and uniform within the outflow volume and non-effective for photon-photon collisions outside this volume. Thus, the opacity due

to γ -ray absorption can be calculated as

$$\tau_{\gamma\gamma}(E_\gamma) = \int_0^{l_{\gamma\gamma}} ds \int_{m_e^2 c^4 / E_\gamma}^\infty d\epsilon \sigma_{\gamma\gamma}(E_\gamma, \epsilon) n_{\text{ph}}(\epsilon, T_b), \quad (22)$$

where, n_{ph} is the photon field of thermal bremsstrahlung radiation given by equation (18), $l_{\gamma\gamma}$ is the length of the path that γ -rays photons travel before leaving the outflow volume, and

$$\sigma_{\gamma\gamma}(E_\gamma, \epsilon) = \frac{\pi r_e^2}{2} (1 - \beta^2) \left[(3 - \beta^4) \ln \left(\frac{1 + \beta}{1 - \beta} \right) + 2\beta(\beta^2 - 2) \right], \quad (23)$$

is the total cross section for photon-photon collisions (e. g., Aharonian et al. 1985, Romero et al. 2010), where $\beta^2 = 1 - m_e^2 c^4 / (E_\gamma \epsilon)$, and r_e is the classical electron radius. The main uncertainty of this approach is the size of the length $l_{\gamma\gamma}$, which depends on the direction of the line of sight as well as on the morphology of the emission region (see Figure 1b).

We show in Figure 3 the attenuation factor $\exp\{-\tau_{\gamma\gamma}\}$ calculated for $l_{\gamma\gamma} = 0.05R_b$ and $2R_b$, (blue solid and dashed curves respectively). Clearly, the difference between these two extreme cases is not substantial for defining the cut-off energy at ~ 30 GeV of the resulting γ -ray flux. The attenuation factors calculated with $l_{\gamma\gamma} = 0.05R_b$ and $2R_b$ are drastically different for γ -rays above 10^{15} eV. However, this difference is irrelevant for all the emission models derived in this work as the maximum energy of the accelerated CR protons (which potentially produce HE γ -rays) is below $\sim 10^{12}$ eV (see subsection 3.2). The attenuation factors displayed in Figure 3 are calculated with the parameters of the model M2, specified in Table 1 and we note the same behaviour discussed above in all the emission models. Thus, for simplicity, we adopt the intermediate value of $l_{\gamma\gamma} = R_b$ for the γ -ray attenuation in all the SED models derived in Section 4.

γ -rays fluxes can also be attenuated by the extragalactic background light (EBL) on the way to the Earth. For a source of red-shift like that of the blazar OJ 287, photon-photon annihilation by the EBL is significant for γ -rays with energies $\gtrsim 100$ GeV (Finke et al. 2010). Since the internal absorption in the emission model discussed here let escape photons with energies $\lesssim 50$ GeV (see Figure 3) we neglect attenuation by the EBL in the SED models derived in Section 3.

3 THE OUTFLOW NON-THERMAL EMISSION

3.1 Conditions for shock formation

Depending on the location of the secondary SMBH impact, the resulting outflow may expand inside or outside a corona of hot gas that surrounds the primary SMBH (see Figure 1a). If the impact takes place within the coronal region, the resulting outflow is unlikely to drive a strong shock as the speed of sound of the coronal gas may be comparable to the expansion velocity of the impact outflow². The scale height

² The electron temperature of an AGN corona may be $T_{c,e} \sim 10^8$ K (Fabian et al. 2015). The proton temperature $T_{c,p}$ in the corona may be two or three orders of magnitudes higher. Considering the temperature of protons, the speed of sound of an isothermal

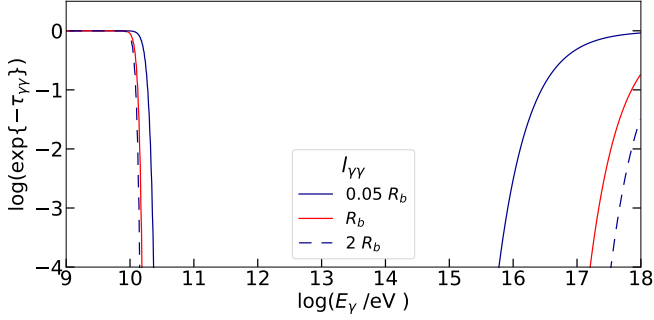


Figure 3. Attenuation factor due to internal γ -ray annihilation in the impact outflow (see the text). The different curves correspond to different lengths assumed for the γ -ray path before leaving the absorption region.

of this putative hot structure surrounding the central BH of AGNs, though model dependent, may be of ~ 10 - $20 R_g$ (Kadowaki et al. 2015; Fabian et al. 2015; Liu et al. 2017), with $R_g = GM/c^2$. For the OJ 287 November 2015 outburst, the SMBH binary model predicts the impact of the secondary SMBH at a distance of $R_{\text{imp}} = 17566 \text{ AU} \sim 100R_g$ from the primary SMBH (Dey et al. 2018), which is outside the central hot corona. Other impact events like those corresponding to the outburst epochs of 1994 and 2005 are predicted closer to the central corona.

Outside the coronal region, the impact outflow may interact with a high velocity AGN wind (driven by the primary SMBH). Observational evidences (e.g. Slone & Netzer 2012; Capellupo et al. 2013) as well as theoretical studies (Melioli & de Gouveia Dal Pino 2015; Giustini & Proga 2019, and references therein) indicate that AGN winds take place in the vicinity of the central engine of AGNs with velocities representing a significant fraction of the speed of light.

A strong shock that accelerate particles can then be formed due to the interaction of the AGN wind and the expanding impact outflow, provided that

$$\mathcal{M}_{\text{sA}} = V_{\text{s0}} \left(c_{\text{w}}^2 + c_{\text{A}}^2 \right)^{-1/2} \gg 1, \quad (24)$$

where the \mathcal{M}_{sA} is the magnetosonic Mach number, $V_{\text{s0}} = c_{\text{s}} + \cos(\theta)V_{\text{w}}$ is the velocity of the AGN wind material in the rest frame of bubble expanding front, V_{w} and c_{s} are the AGN wind and the bubble expansion velocities, respectively (see equation 19), in the frame of the primary SMBH, θ is the angle between the wind velocity and the vector $-\hat{n}$, being \hat{n} the unit vector normal to the shock surface (see Figure 1b), and c_{w} and c_{A} are the sonic and Alfvénic speeds, of the AGN wind respectively. Using $c_{\text{w}}^2 = \gamma_{\text{w}}kT_{\text{w}}/m_{\text{p}}$ and $c_{\text{A}}^2 = B_{\text{w}}^2/(4\pi m_{\text{p}}n_{\text{w}})$ where T_{w} , n_{w} , and B_{w} are the temperature, number density, and magnetic field of the AGN wind, the

corona may then be of $\sim 0.095c (T_{\text{c,p}}/10^{11}\text{K})^{1/2}$ which is comparable to the expansion velocity c_{s} of the impact outflow (see equation 19).

magnetosonic Mach number can be estimated as:

$$\begin{aligned} \mathcal{M}_{\text{sA}} &= V_{\text{s0}} \left(\frac{m_{\text{p}}}{\gamma_{\text{w}}kT_{\text{w}}} \right)^{1/2} \left(1 + \frac{B_{\text{w}}^2}{4\pi\gamma_{\text{w}}kT_{\text{w}}n_{\text{w}}} \right)^{-1/2} \\ &\sim 13.9 \left(\frac{V_{\text{s0}}}{0.2c} \right) \left(\frac{10^9\text{K}}{T_{\text{w}}} \right)^{1/2} \times \\ &\quad \left[1 + 0.3 \left(\frac{B_{\text{w}}}{1\text{G}} \right)^2 \left(\frac{10^9\text{K}}{T_{\text{w}}} \right) \left(\frac{10^6\text{cm}^{-3}}{n_{\text{w}}} \right) \right]^{-1/2}, \end{aligned} \quad (25)$$

where we use $\gamma_{\text{w}} = 5/3$.

If the shock is radiation-dominated, the appropriate specific heat ratio for the gas within the shock is $\gamma_{\text{sh}} = 4/3$ and the maximum shock compression is 7. Alternatively, if the shock is optically thin, radiation fields (originated within the shell or externally) produce no substantial effects on the properties of the shocked gas. In this case $\gamma_{\text{sh}} = 5/3$ is the appropriate value for the specific heat ratio which leads to a maximum compression of 4. The shocked material is optically thin as long as the time scale of photon diffusion $t_{\text{diff}} = \tau R_{\text{b}}/c = \sigma_{\text{T}}n_{\text{sh}}R_{\text{b}}^2/c$ (i.e., the time that photons take to leave the swept up shell) is much shorter than the time scale of the outflow expansion $t_{\text{exp}} \sim R_{\text{b}}/v_{\text{r}}$ (here we consider the initial outflow velocity $\sim v_{\text{r}}$ as the maximum velocity of the expansion, see equation 19). Thus, the shock formed by the interaction of the AGN wind and the outflow bubble is optically thin if gas number density of the shocked gas is

$$n_{\text{sh}} \ll \frac{c}{v_{\text{r}}\sigma_{\text{T}}R_{\text{b}}} \sim 5 \times 10^8 \text{cm}^{-3} \left(\frac{0.1c}{v_{\text{r}}} \right) \left(\frac{0.01\text{pc}}{R_{\text{b}}} \right). \quad (26)$$

As we will see in Section 4, in all the emission models considered in this paper the parameters of wind-outflow shock fall in the optically thin regime.

We compare the associated mechanical luminosity of the AGN wind with the mass accretion power of the primary SMBH by defining the wind efficiency parameter

$$\eta_{\text{w}} \equiv \frac{\pi R_{\text{imp}}^2 \rho_{\text{w}} V_{\text{w}}^3}{\dot{M}_1 c^2} = 0.28 \left(\frac{n_{\text{w}}}{5 \times 10^6 \text{cm}^{-3}} \right) \left(\frac{V_{\text{w}}}{0.25c} \right)^3. \quad (27)$$

In this ratio, we use $R_{\text{imp}} = 17566 \text{ AU}$ for the distance of the secondary SMBH-disc impact (corresponding to the 2015 outburst, see Dey et al. 2018) and $\dot{M}_1 = 0.12\dot{M}_{\text{Edd}}$ for the mass accretion rate of the primary SMBH of OJ 287 (Valtonen et al. 2019).

According to the estimations discussed in this subsection, a strong shock can be formed due to the interaction of the AGN wind and the impact outflow, if the AGN wind has velocity, temperature, magnetic field, and gas density constrained to values $V_{\text{w}} \gtrsim 0.2c$, $T_{\text{w}} \lesssim 10^9 \text{K}$, $B_{\text{w}} \lesssim 1\text{G}$, and $n_{\text{w}} \gtrsim 10^6 \text{cm}^{-3}$, respectively. In the next subsection, we assume that such an AGN wind exists above the accretion disc at the location of the secondary SMBH impact and then we derive the associated non-thermal, hadronic emission of the accelerated CR protons.

We consider the total energy of the emitting CR protons to be a small fraction of the kinetic wind energy E_{w} that crosses the shock formed due to the interaction of the AGN wind and the expanding outflow (see equation 39 in the next subsection). We calculate the impinging wind energy E_{w} assuming for simplicity an AGN wind with local

plane-parallel geometry of uniform density ρ_w and velocity V_w . Considering the surface of the forward shock as nearly spherical, the flux of wind kinetic energy impinging on the shock surface can be estimated as

$$\frac{dE_w}{dt dA} = \frac{1}{2} \rho_w [c_s + \cos(\theta) V_w]^3, \quad (28)$$

where θ is the angle between the wind velocity and the vector $-\hat{n}$, being \hat{n} the unit vector normal to the surface of the shock (see Figure 1b). Thus, the wind kinetic energy that crosses the shock front during the time Δt_b (which corresponds to the period when the outflow bubble expands from the R_0 to R_b), can be calculated as

$$E_w = \int_0^{\Delta t_b} dt R(t)^2 \int_0^{2\pi} d\phi \int_0^{\pi/2} d\theta \sin(\theta) \frac{dE_w}{dt dA}. \quad (29)$$

Integrating equation (29) with Δt_b , $c_s(t)$, and $R(t)$ given by equations (19)-(21) (corresponding to an expanding bubble according to Lehto & Valtonen 1996) gives

$$E_w = \pi \rho_w R_0^3 \left[\frac{c_{s,0}^2}{2} (\xi^2 - 1) + \frac{3}{5} c_{s,0} V_w (\xi^{5/2} - 1) + \frac{V_w^2}{3} (\xi^3 - 1) + \frac{V_w^3}{14 c_{s,0}} (\xi^{7/2} - 1) \right]. \quad (30)$$

R_0 and ξ and $c_{s,0}$ can be obtained as described in Section 2.1. We employ ρ_w and V_w as free parameters that are found by matching the calculated emission of hadronic origin to the observed X-ray and γ -ray data (see the Section 4). In reality, the shock formed due to the collision of the outflow bubble and the AGN wind may follow a bow-shock morphology (as depicted in Figure 1b). Therefore, equation (29) slightly underestimates the wind kinetic energy impinging on the shock surface.

3.2 Emission from proton-proton interactions

To calculate the potential non-thermal radiation produced by the impact outflow, we consider acceleration of CRs in the shock formed by the interaction of the expanding bubble with the AGN wind driven by the primary SMBH (see Figure 1). Assuming diffusive shock acceleration (DSA), the acceleration rate of CR protons can be written as

$$t_{\text{acc}}^{-1} = \frac{1}{E} \frac{dE}{dt} = \frac{V_{s0}^2}{D(E)}, \quad (31)$$

where V_{s0} is the upstream velocity in the co-moving frame of the shock (see the previous subsection), and D is the CR diffusion coefficient in the acceleration region. Since super-Alfvénic turbulence is likely to develop in the super-Alfvénic, supersonic AGN wind, we adopt for simplicity a spatially uniform, Kolmogorov-like diffusion coefficient of the form (Ptuskin et al. 2006; Celli et al. 2019):

$$D = D_0 \left(\frac{E}{E_0} \right)^{1/3} \left(\frac{B}{B_0} \right)^{-1/3} \quad (32)$$

with $E_0 = m_p c^2 + 2m_\pi c^2 + m_\pi^2 c^4 / (2m_p c^2) = 1.22$ GeV (the threshold energy for the production of π^0 mesons), $B_0 = 1$ G, and we choose the normalisation constant $D_0 = 5 \times 10^{25}$ cm² s⁻¹. This form of the diffusion coefficient is motivated by the condition

$$\sqrt{2D\Delta t_b} > \Delta R, \quad (33)$$

in which CRs protons with energies $> E_0$ diffuse from the forward shock into the bubble in a time $< \Delta t_b$. Here Δt_b is the time that the bubble takes to produce the optical outburst (see equation 21), and $\Delta R \sim 0.5R_b$ is the thickness of the shell³ of shocked AGN wind material (region ii in Figure 1b). With this normalisation, for $B = 1$ μ G and $E = 10$ GeV, equation (32) gives $D \sim 10^{28}$ cm² s⁻¹ which, coincidentally, is of the order of the average diffusion coefficient inferred for our Galaxy.

Given the radius R_b , density n_b , temperature T_b , and photon field n_{ph} of the outflow bubble, the magnetic field B in the acceleration region required to accelerate CR protons up to a maximum energy E_{max} can be found by balancing the acceleration rate t_{acc}^{-1} with the rates of energy losses of protons in the swept up shell (region ii in Figure 1b):

$$t_{\text{acc}}^{-1}(E_{\text{max}}, B) = t_{\text{diff}}^{-1}(E_{\text{max}}, B) + t_{\text{pp}}^{-1}(E_{\text{max}}, n_b) + t_{\text{py}}^{-1}(E_{\text{max}}, n_{\text{ph}}). \quad (34)$$

In this equation, we consider the energy loss rates due to CR diffusion t_{diff}^{-1} , proton-proton interactions t_{pp}^{-1} (of CRs with the thermal protons in the swept up shell), and photo-pion production t_{py}^{-1} (due to interactions of CRs with the thermal bremsstrahlung radiation of the expanding bubble, see equation 18). We note that these cooling rates change as the outflow bubble evolves. For the sake of simplicity, we calculate these cooling rates at the time when the outflow bubble allows the thermal bremsstrahlung photons to escape (see Section 2.1). The expressions that we employ for the rate terms in equation (34) are described in Appendix (B). In Figure 4a, we plot the characteristic times as a function of the proton energy of the acceleration and energy loss rates of protons in the swept up shell with parameters corresponding to a particular emission model derived in Section 4 (the model M2, see also Table 1).

Considering that CRs protons escape isotropically from their acceleration zone, we note that the material of the outflow bubble (see Figure 1b) is the main target for p - p interactions (of CR protons with the local thermal ions). For the parameters of the emission models considered here, these interactions occur much more efficiently within the outflow bubble than within the shell of swept up material. This can be seen by comparing the p - p cooling time curves (orange) in the upper and lower panels of Figure 4. These curves are the p - p cooling times in the shell of shocked AGN wind and in the region within outflow bubble, respectively. For an AGN wind with gas density $n_w \sim 5 \times 10^6$ cm⁻³, for instance, CR protons with energies of ~ 1 TeV cools via p - p interactions within the swept up shell in a time scale of years. By contrast, the p - p cooling time of CR protons within an outflow bubble of gas density $\sim 10^{10}$ cm⁻³ is of few days.

The neutral and charged pions (π^0 and π^\pm) produced

³ For a plane-parallel wind impinging on a spherical surface with sonic Mach number $\gg 1$, the thickness of the swept up shell at $\theta = 0$ (see Figure 1b) can be well approximated as $\Delta R \sim \epsilon(0.76 + 1.05\epsilon^2)R_b \sim 0.2R_b$, where $\epsilon = (\gamma - 1)/(\gamma + 1) = 1/4$, for $\gamma = 5/3$ (Verigin et al. 2003, their equation 22). At $\theta = \pi/2$, this thickness is $\Delta R \sim 0.75R_b$ (Verigin et al. 2003, their Figure 4). In the condition (33), we employ the intermediate value of $\Delta R = 0.5R_b$.

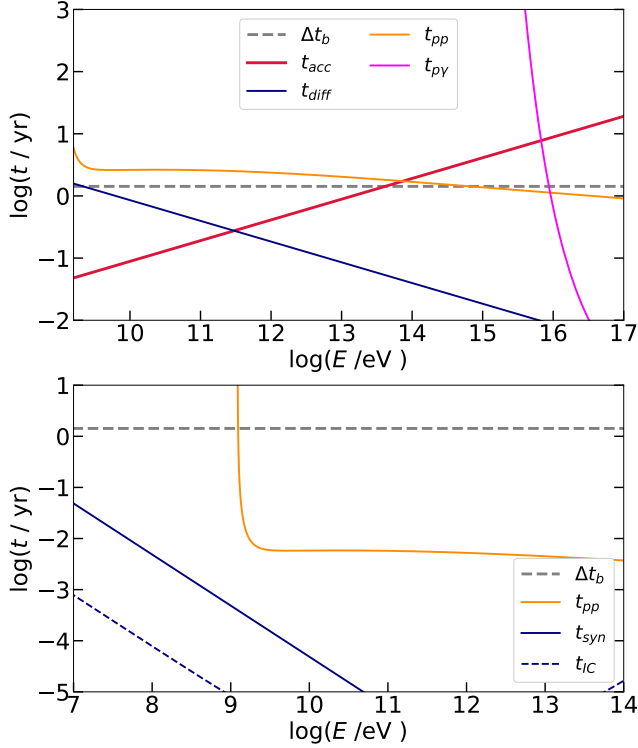


Figure 4. Upper: Characteristic times of acceleration and cooling for CR protons in the shell of swept up material (region ii in Figure 1b) driven by the impact outflow (see the text). Lower: Cooling times for protons and secondary e^\pm pairs within the outflow bubble (region iii in Figure 1b; see the text). The curves in these panels correspond to the parameters of the emission model M2 (see Table 1).

out of p - p interactions decay into γ -rays and electron-positron pairs e^\pm through the channels:

$$\pi^0 \rightarrow \gamma + \gamma, \quad (35)$$

$$\pi^\pm \rightarrow \mu^\pm + \nu_\mu(\bar{\nu}_\mu), \quad (36)$$

$$\mu^\pm \rightarrow e^\pm + \bar{\nu}_\mu(\nu_\mu) + \nu_e(\bar{\nu}_e), \quad (37)$$

where μ^\pm and ν_s represent muons and neutrinos, respectively. For the time scales of the problem discussed here, we can assume that pions and muons decay instantaneously in the primary SMBH rest frame. In all the emission models derived in Section 3, the secondary e^\pm pairs cool down more efficiently due to IC scattering (of the thermal bremsstrahlung radiation field generated by the outflow bubble) than due to synchrotron radiation. This is illustrated with the cooling times of e^\pm displayed in Figure 4b, corresponding to the emission model M2 (specified in Table 1).

To calculate the emission due to π^0 decay as well as due to the secondary e^\pm pairs generated out of p - p interactions, we first assume that a stationary population of CRs has been injected within the volume of the outflow bubble. The volume that this CR population occupies within the bubble (region iii in Figure 1b) can be estimated according to the distance that CRs protons diffuse in a time Δt_b (the time that the outflow bubble takes to manifest as a flare). Employing the diffusion coefficient defined in equation (32), the distance that the CRs penetrates within the bubble is

$\Delta d \sim \sqrt{2D(E, B)\Delta t_b} - \Delta R$, where $\Delta R \sim 0.5R_b$ is the thickness of the shell of AGN wind shocked material (region ii in Figure 1). For a background magnetic field of $B = 5$ G and $R_b = 96$ AU for instance (corresponding to the emission model M2, see Table 1), the penetration depth Δd of CR protons with energies between 1.22 GeV and 300 GeV, is in the range of $0.4R_b \lesssim \Delta d \lesssim 1.8R_b$. In this case the accelerated CR protons occupy almost the whole volume of the bubble.

We parameterise the energy distribution of the CR population within the bubble as a power-law (P-L) with exponential cut-off of the form

$$J_p(E_p) = A \left(\frac{E_p}{E_0} \right)^{-q} \exp \left\{ -\frac{E_p}{E_{\max}} \right\} \text{ erg}^{-1} \text{ cm}^{-3}, \quad (38)$$

where E_p is the energy of the CR protons (rest mass plus kinetic energy), $E_0 = 1.22$ GeV (the threshold energy for π^0 mesons), E_{\max} is the maximum energy of the accelerated protons. The normalisation constant A is obtained through the condition

$$0.1E_w = \int_V dV \int_{E_{\min}}^{\infty} dE E J_p(E). \quad (39)$$

In this condition, we fix the total energy of the CR population to be one tenth of the kinetic wind energy that impinges the surface of the shock formed by the AGN wind and the outflow bubble during its expansion from R_0 until R_b (see equation 29). This 10% efficiency is motivated by the energy fraction of galactic supernovae needed to explain the galactic CR density (Longair 2011), as well as results of numerical simulations of particle acceleration by DSA (see e. g. Caprioli & Spitkovsky 2014).

The volume integral in the RHS of equation (39) is simplified assuming that the distribution J_p is uniform along the volume V of CR emission. With this consideration, the normalisation constant of the CR distribution (38) is given by

$$A = \frac{0.1E_w}{E_0^q V I_p} \text{ erg}^{-1} \text{ cm}^{-3}, \quad (40)$$

where $I_p(E_0, E_{\max}, q) = \int_{E_0}^{\infty} dE E^{1-q} \exp\{-E/E_{\max}\}$.

The observed flux of γ -rays due to the decay of neutral pions produced by the CR population (38) in the outflow bubble of OJ 287 is calculated as

$$\nu F_{\nu, \pi^0} = \frac{V}{4\pi D_L^2} E'^2 \Phi_\gamma(E') \exp\{-\tau_{\gamma\gamma}(E')\}, \quad (41)$$

where $E' = h\nu(z+1)$, being $z = 0.306$ the redshift of the source, $D_L = 1602$ Mpc the luminosity distance, V the volume occupied by the CR injected within the outflow bubble, and $\tau_{\gamma\gamma}$ is the optical depth of photon-photon annihilation within the source given by equation (22). In equation (41), Φ_γ is the γ -ray production rate (photons per unit energy, per unit time, per unit volume) in units of $\text{erg}^{-1} \text{ s}^{-1} \text{ cm}^{-3}$. For γ -rays produced by CRs with energies > 100 GeV we calculate the function Φ_γ employing the parametrisation derived by Kelner et al. (2006):

$$\Phi_{\gamma, h}(E') = cn_b \int_{E_\gamma}^{\infty} \sigma_{pp}(E_p) J_p(E_p) F_\gamma(E'/E_p, E_p) \frac{dE_p}{E_p}, \quad (42)$$

where n_b is the gas number density of the thermal ions within the outflow bubble (see equation 7), σ_{pp} is the total cross section for p - p interactions given Kelner et al. (2006)

(their equation 79), J_p is the energy density distribution of CR protons defined in equation (38), and the function $F_\gamma(E'/E_p, E_p)$ is defined in equation (58) of Kelner et al. (2006).

For γ -rays produced by CRs with energies ≤ 100 GeV, we calculate the γ -ray production rate as:

$$\Phi_{\gamma,1}(E') = \frac{2c\tilde{n}_\gamma n_b}{\tilde{K}_{pp}} \int_{E_{\min\pi^0}}^{\infty} \frac{\sigma_{pp}(y)J_p(y)}{\sqrt{E_\pi^2 - m_\pi^2 c^4}} dE_\pi, \quad (43)$$

which is a modified version of the δ -functional approach of (Aharonian & Atoyan 2000) suggested in (Kelner et al. 2006). In equation (43), $E_{\min\pi^0} = E' + m_{\pi^0}^2 c^4 / (4E')$, being m_{π^0} the mass of the neutral pion, and $y \equiv m_p c^2 + E_\pi / \tilde{K}_{pp}$. Following (Kelner et al. 2006), $\tilde{K}_{pp} = 0.17$ is taken as a fixed parameter (which agrees quite well with numerical Monte Carlo calculations at energies ~ 1 GeV), and \tilde{n}_γ (interpreted as the multiplicity of neutral pion production) is obtained by requiring the functions $\Phi_{\gamma,1}$ and $\Phi_{\gamma,h}$ to match at $E' = 0.1$ TeV:

$$\tilde{n}_\gamma(q, E_{\max}) = \frac{\tilde{K}_{pp}}{2} \times \int_{0.1\text{TeV}}^{\infty} \sigma_{pp}(E_p) J_p(E_p, q, E_{\max}) F_\gamma(0.1\text{TeV}/E_p, E_p) \frac{dE_p}{E_p} \times \left[\int_{0.1\text{TeV} + m_{\pi^0}^2 c^4 / 0.4\text{TeV}}^{\infty} \frac{\sigma_{pp}(y)J_p(y)}{\sqrt{E_\pi^2 - m_\pi^2 c^4}} dE_\pi \right]^{-1}. \quad (44)$$

To calculate the synchrotron and IC emission produced by the secondary e^\pm pairs (see Eq. 37), we model the energy distribution $N_e(E_e)$ of these leptons (in units of $\text{erg}^{-1} \text{cm}^{-3}$) as a stationary solution of the transport equation (e.g., Ginzburg & Syrovatskii 1964) for the population of e^\pm pairs within the p - p emission region:

$$N_e(E_e) = |P_e|^{-1} \int_{E_e}^{\infty} dE'_e \Phi_e(E'_e). \quad (45)$$

The factor P_e in equation (45) is the total rate of e^\pm energy losses:

$$P_e = P_{\text{syn}} + P_{\text{IC}} + P_{\text{br}} + P_{\text{Co}}, \quad (46)$$

where we consider losses due to synchrotron radiation, IC scattering, relativistic bremsstrahlung, and Coulomb collisions, respectively (the expressions for these cooling terms can be found in Appendix C). The function Φ_e within the integral of equation (45) is the e^\pm production rate in units of $\text{erg}^{-1} \text{s}^{-1} \text{cm}^{-3}$ (particles per unit energy, per unit time, per unit volume). For leptons produced by CR protons with energies > 0.1 TeV, we calculate the function Φ_e employing the parametrisation derived by Kelner et al. (2006):

$$\Phi_{e,h}(E_e) = cn_b \int_{E_e}^{\infty} \sigma_{pp}(E_p) J_p(E_p) F_e(E_e/E_p, E_p) \frac{dE_p}{E_p}, \quad (47)$$

and for leptons produced by CR protons with energies ≤ 0.1 TeV we employ the δ -functional approach (see Kelner et al. 2006):

$$\Phi_{e,1}(E_e) = \frac{2cn_b \tilde{n}_e}{\tilde{K}_{pp}} \int_{E_{\min\pm}}^{\infty} \sigma_{pp}(y) J_p(y) f_e(E_e/E_\pi) \frac{dE_\pi}{E_\pi}, \quad (48)$$

similarly as done in the calculations of Petropoulou et al. (2016). In equation (48), $E_{\min\pm} = E_e + (m_{\pi^\pm} c^2)^2 / (4E_e)$,

where m_{π^\pm} is the mass of charged pions. The functions $F_e(E_e/E_p, E_p)$ and $f(E_e/E_\pi)$ in equations (47) and (48) are defined by equations (62) and (36) of Kelner et al. (2006), respectively. Similarly as in the case case for γ -ray production, we set $\tilde{K}_{pp} = 0.17$ and the factor \tilde{n}_e in equation (48) is obtained from the condition $\Phi_{e,h}(E_e = 0.1 \text{ TeV}) = \Phi_{e,1}(E_e = 0.1 \text{ TeV})$.

Once the stationary distribution (45) is computed, we apply it to calculate the synchrotron and IC fluxes following the usual prescriptions (e.g., Blumenthal & Gould 1970, Romero et al. 2010). The flux of synchrotron radiation at the Earth is then calculated as:

$$\nu F_{\nu,\text{syn}} = \frac{V}{4\pi D_L^2} E' \int_{E_{\min,e}}^{E_{\max,e}} dE_e N_e(E_e) \langle P_{\text{syn}} \rangle_\alpha \quad (49)$$

where $\langle P_{\text{syn}} \rangle_\alpha = \frac{1}{2} \int_0^\pi \sin \alpha P_{\text{syn}} d\alpha$ is the synchrotron emission power, averaged over the pitch angle α ,

$$P_{\text{syn}}(E_e, E', \alpha, B) = \frac{\sqrt{3}e^3 B \sin \alpha}{hm_e c^2} \frac{E'}{E_c} \int_{E'/E_c}^{\infty} K_{5/3}(x) dx, \quad (50)$$

$K_{5/3}(x)$ is the modified Bessel function of order 5/3, and

$$E_c = \frac{3}{4\pi} \frac{ehB \sin \alpha}{m_e c} \left(\frac{E_e}{m_e c^2} \right)^2. \quad (51)$$

In equations (50) and (51), B is the magnetic field in the hadronic emission region (region iii in Figure 1b) which we assume to have the same value as in the acceleration region (region ii in Figure 1b).

For the emission due to IC scattering of the secondary electron-positron pairs, we consider as seed photons the thermal radiation of the outflow bubble. Thus, we calculate the observed flux of IC emission as

$$\nu F_{\nu,\text{IC}} = \frac{V}{4\pi D_L^2} \exp\{-\tau_{\gamma\gamma}(E')\} \times E'^2 \int_{E_{\min,e}}^{E_{\max,e}} dE_e N_e(E_e) \int_{\epsilon_{\min}}^{\epsilon_{\max}} d\epsilon P_{\text{IC}}(E', E_e, \epsilon), \quad (52)$$

with

$$P_{\text{IC}} = \frac{3\sigma_T m_e^2 c^5}{4E_e^2} \frac{n_{ph}(\epsilon, T_b)}{\epsilon} F(E', E_e, \epsilon). \quad (53)$$

In equation (52), $N_e(E_e)$ is the energy distribution of electron-positron pairs calculated with equation (45). In equation (53), $n_{ph}(\epsilon, T_b)$ is the photon field generated by the thermal radiation within the outflow bubble of temperature T_b given by equation (18), and

$$F(E', E_e, \epsilon) = 2q \ln q + (1 + 2q)(1 - q) + \frac{1}{2}(1 - q) \frac{(\Gamma q)^2}{1 + \Gamma q}, \quad (54)$$

$$q = \frac{E'}{\Gamma(E_e - E')},$$

$$\Gamma = \frac{4\epsilon E_e}{m_e^2 c^4},$$

where the energy of the scattered photons is in the range $\epsilon \leq E' \leq E_e \Gamma / (1 + \Gamma)$. We note that to calculate the fluxes due to pion decay, synchrotron and IC scattering of secondary e^\pm with equations (41), (49), and (52), it is not needed to explicitly specify the volume V of the hadronic emission region within the outflow bubble. This is because, according to the normalisation condition of equation (39), the energy

distributions of CR protons and electron-positron pairs are $J_p \propto V^{-1}$ and $N_e \propto V^{-1}$, which cancel the volume factor in equations (41), (49), and (52).

In the next Section, we apply the non-thermal and thermal emission processes described in this and the previous section, to model the observed MW SED corresponding to the November 2015 flare of OJ 287.

4 SED MODELS FOR THE 2015 MAJOR FLARE OF THE BLAZAR OJ 287

Following its historical ~ 12 year optical flares, OJ 287 displayed a major optical excess in November 2015 in agreement with the prediction of the SMBH binary model (Valtonen et al. 2016).

In the X-ray and γ -ray bands, flare activity was also reported. Kushwaha et al. (2018b) carried out a MW analysis of the LCs during and after the November 2015 flare finding significant activity most prominently in the NIR, optical, UV and X-ray bands, associated with significant change in the polarisation angle (PA) and polarisation degree (PD; see also Gupta et al. 2019). Kushwaha et al. (2018b) extracted the MW SED of the flare and interpreted the X-ray and γ -ray components in terms of leptonic jet emission (they find X-rays consistent with SSC with EC) whereas γ -ray data are better explained with EC), and the optical component in terms of multi-temperature disc emission.

Here, we present an alternative model for the SED extracted by Kushwaha et al. (2018b). Motivated by the fact that the LCs in the X-ray and γ -ray bands display flaring simultaneously with the optical excess, we interpret this flare state in terms of the BH-disc impact scenario described in Sections 2-3. To do this, we first determine the properties of the outflow bubble (R_b , n_b , T_b , and n_{ph}) when the outburst occurs. This is done by matching the thermal bremsstrahlung emission of the bubble with the optical flare data using v_r , n_d , and f_R as free parameters (see Section 2.1). Then, we calculate the non-thermal emission of the outflow bubble with the hadronic emission model described in Section 3.2.

To define the magnetic field B in the acceleration region, some features of the broadband flare data together with the model described in Section 3.2 offer the following constraints. (i) We note that the magnetic field B in the acceleration region must be high enough to accelerate CR protons up to an energy E_{max} able to produce γ -ray photons of at least ~ 5 GeV, the highest energy of the γ -ray data. This is a lower limit for E_{max} , since γ -ray photons with energies much higher than ~ 5 GeV could be produced but not seen due to photon-photon annihilation (see Section 2.2). (ii) The magnetic field must be able to cool the secondary $e\pm$ pairs enough (by synchrotron losses) for these leptons to not over-produce X-ray photons by IC scattering. (iii) At the same time, the magnetic field should be low enough to produce a negligible flux of synchrotron radiation at optical energy bands. This last condition is imposed by the initially low PD observed in the optical outburst. Thus, once we obtain the outflow bubble properties (R_b , T_b , n_b , n_{ph}), we use E_{max} as a free parameter to derive the magnetic field B through the balance equation (34) (for acceleration and cooling rates of CR protons). With this procedure, we seek for parameter

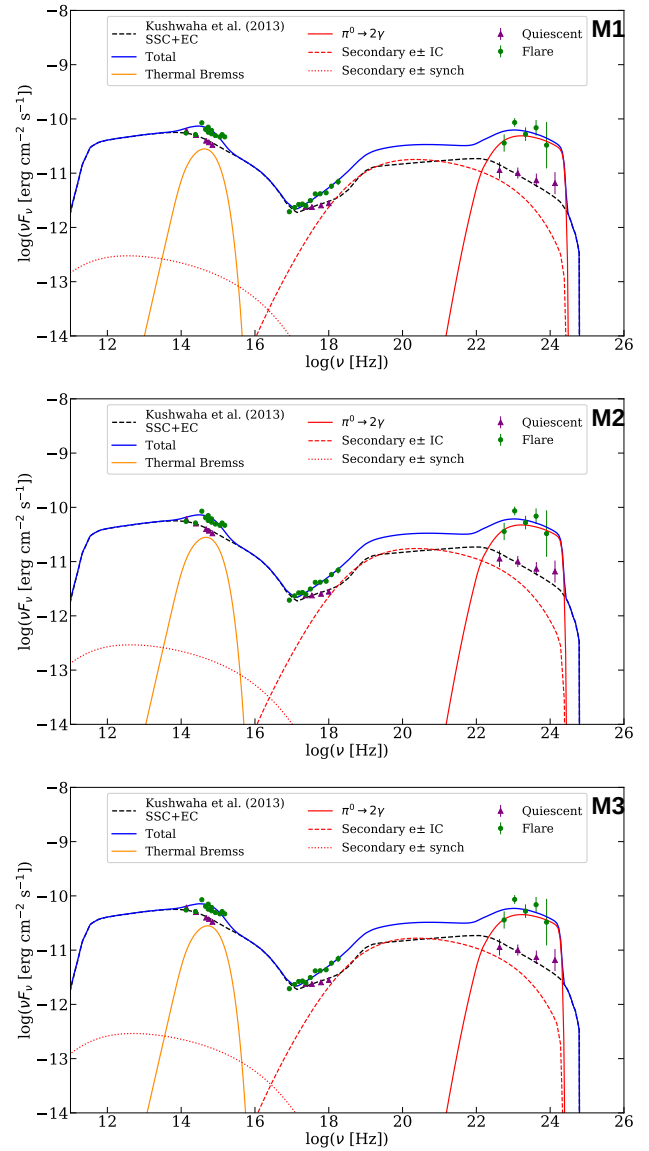


Figure 5. Flare and quiescent SEDs of the blazar OJ 287. The flare data (green points, adapted from Kushwaha et al. 2018b) corresponds to the period MJD: 57359-57363 (simultaneous to the November 2015 optical major flare). The data of the quiescent state (magenta points, adapted from Kushwaha et al. 2013) corresponds to the period MJD: 55152-55184. The over-plotted curves are emission models for the quiescent (black dashed curve, adapted from Kushwaha et al. 2013) and flare state (blue solid curve). The red and orange curves are the components of the flare thermal+hadronic emission model derived in this paper (see the text). The three panels display the same data points and the same quiescent emission model, whereas a different flare emission profile is displayed in each panel. The model parameters of the flare emission profiles (labelled as M_i) are listed in Table 1.

configurations implying broadband SEDs fulfilling the conditions listed above and at the same time requiring an AGN wind power as low as possible.

The green data points in the plots of Figure 5 are the flare MW SED extracted from the LCs data corresponding to MJD: 57359-57363 (see Kushwaha et al. 2018b). The data

Table 1. Free and derived parameters for the SEDs profiles of the models M1, M2 and M3 displayed in Figure 5. (See more details in the text.)

		M ₁	M ₂	M ₃
Free	$n_d [10^{14} \text{cm}^{-3}]$	1.00	1.00	1.00
	$(v_r/c) \times 10$	1.54	1.62	1.70
	f_R	0.85	0.85	0.85
	$n_w [10^6 \text{cm}^{-3}]$	6.50	6.50	6.50
	$T_w [10^9 \text{K}]$	1.00	1.00	1.00
	$(V_w/c) \times 10$	2.20	2.50	2.80
	q	2.20	2.20	2.20
	$E_{\text{max}} [\text{TeV}]$	0.30	0.30	0.30
Derived	$T_0 [10^6 \text{K}]$	1.05	1.08	1.10
	$R_0 [\text{AU}]$	106.57	96.30	87.46
	$\xi = R_b/R_0$	42.44	39.05	36.08
	$\Delta t_b [\text{yr}]$	1.88	1.43	1.09
	$n_b [10^{10} \text{cm}^{-3}]$	0.92	1.18	1.49
	$T_b [10^4 \text{K}]$	2.47	2.76	3.06
	$\frac{L_w}{M_1 c^2} \times 10$	2.46	3.61	5.07
	$B [\text{G}]$	4.20	5.08	6.20
	\mathcal{M}_{sA}	10.63	11.85	12.97
	$E_{\text{CR}} [10^{52} \text{erg}]$	4.75	3.59	2.70

points in magenta represent the SED of what we consider as the pre-burst, quiescent state, for which we take the SED data extracted by Kushwaha et al. (2013) corresponding to the 2009 broadband LCs of the source (their “state 3” data, when no significant variability was displayed). The flare data (green points) are from: *Fermi*-LAT (Atwood et al. 2009) at γ -ray energies, *Swift*-XRT (Burrows et al. 2005) at X-rays, and *Swift*-UVOT + 11 ground-based observatories (Gupta et al. 2017; Kushwaha et al. 2018b). Similarly for the quiescent state data (magenta points).

In Figure 5, we overplot different SED emission profiles that result from the thermal+hadronic emission model and the parameters associated to each model are listed in Table 1. The blue curve is the calculated total emission that results from the quiescent plus the flare components. The quiescent state is a SSC + EC jet emission model (black, dashed curve), which here we adapt from Kushwaha et al. (2013). The orange solid curve is the outburst thermal bremsstrahlung emission (described in Section 2), whereas the red curves represent the flare emission of hadronic origin (see Section 3.2). The red solid curve corresponds to π^0 decay emission. The red dotted and dashed curves correspond to synchrotron and IC fluxes of the secondary e^\pm pairs, respectively. In all the models derived here, the thermal bremsstrahlung radiation is more intense, by two orders of magnitude or more, than the synchrotron radiation gener-

ated by the e^\pm pairs. Because of this, we neglect the SSC contribution, and thus we employ the thermal bremsstrahlung photon field given by equation (18) as the dominant source of seed photons for IC scattering.

The models M1, M2, and M3 share the same assumed free parameters with the exception of v_r (the velocity of the disc material relative to the secondary SMBH at the impact event) and V_w (the AGN wind velocity). We note that the emission models are most sensitive to the variations of v_r . For larger v_r , a larger AGN wind power is required to match the HE data. Adopting different values of v_r and V_w we generate emission profiles consistent with the broadband data which result in outflow bubbles with noticeable different properties (see the derived parameters in the second section of Table 1).

In all the models presented in Figure 5, the synchrotron emission of the secondary e^\pm pairs does not contribute substantially to any spectral region of the flare data. This is particularly consistent with the low PD initially observed in the optical flare. We also see that the X-ray and γ -ray spectral components are consistent with a CR population (within the outflow bubble) of P-L index $q = 2.2$ and maximum energy $E_{\text{max}} = 0.3$ TeV.

According to the displayed emission models, to reproduce the HE flare SEDs, an AGN wind representing $\lesssim 50\%$ of the primary SMBH accretion power is required (according to the definition in equation 27). Considering energy efficiency, the model M1 appears to be the most favoured.

5 SUMMARY AND DISCUSSION

The BL Lac blazar OJ 287 displayed a major optical outburst in November 2015, in agreement with its well known ~ 12 yr optical periodicity. Simultaneous flaring was also reported in the X-ray and γ -ray bands, with hardening in the spectral index compared with previous states seen in this source (Kushwaha et al. 2018b). In the present work, we show that a hadronic emission component compatible with the presence of a SMBH binary system in the core of OJ 287 reproduces the X-ray and γ -ray data self-consistently with a thermal component constrained by the optical outburst.

The one-zone thermal+hadronic emission model presented here is based on the following considerations.

- The secondary SMBH impacts the accretion disc of the primary one, generating a bipolar outflow (Ivanov et al. 1998; Pihajoki 2016). The outflow that emerges the accretion disc in the direction of the observer is the dominant source of the observed emission. We model this outflow following Lehto & Valtonen (1996), considering it as a spherical bubble that grows at the speed of sound of the internal gas.
- CR protons are accelerated in the forward shock formed by the expanding outflow bubble as it collides with the local AGN wind (see Section 3).
- By the time of the optical outburst a population of CR protons has been injected within the outflow bubble (see Figure 1b). This CR population has a total energy representing one tenth of the AGN wind kinetic energy that impinged on the outflow bubble during its expansion. We then calculate the π^0 decay emission as well as synchrotron and IC scattering of secondary e^\pm pairs, where the neutral pions and secondary leptons are generated out of p - p interac-

tions (Aharonian & Atoyan 2000; Kelner et al. 2006). The dominant seed photon field for IC scattering is the thermal bremsstrahlung radiation of the outflow bubble (see Section 3).

We present different emission profiles which can explain the observed flare data. The inferred magnetic field in the acceleration region of these emission models is in the range of $\sim 4 - 6$ G. The CR population responsible for the X-ray and γ -ray components is consistent with a P-L index $q \sim 2.2$ and a cut-off energy of ~ 0.3 TeV. In all the derived models, the mechanical luminosity of the AGN wind represents $\lesssim 50\%$ of the mass accretion power of the primary SMBH (see Table 1).

To interpret the emission data with the one-zone hadronic emission model discussed here, we assumed values for the size of the corona region as well as for the parameters of the AGN wind which appear to be reasonable and according to previous studies of coronae and wind of AGNs (see Section 3.2). However, more realistic models for the corona and the AGN wind (which are beyond the scope of this paper) could, perhaps, modify the results obtained here. For instance, the maximum energy E_{\max} of accelerated protons by DSA depends on the velocity and magnetic field of the wind impinging on the outflow bubble. Also, due to the precessing nature of the secondary SMBH orbit, the BH-disc impacts are expected to occur at different radii from the primary SMBH (see e. g. Dey et al. 2018) and DSA would not be efficient for BH-disc impacts occurring closer (or inside) to the primary SMBH AGN corona (see Section 3.1). Such study of whether or not closer impacts produce observable HE emission, we leave for a future work.

The acceleration, propagation and emission of CRs within the source depend on the diffusion of these relativistic particles. For simplicity, here we adopted a spatially uniform, Kolmogorov-like diffusion coefficient (see Section 3.2). Nevertheless, more elaborate scenarios for CR diffusion could lead to more efficient particle acceleration, implying higher maximum energies for CR protons and detectable fluxes of HE neutrinos⁴. For example, enhanced turbulence is expected to develop behind the forward shock (Giacalone & Jokipii 2007; Mizuno et al. 2014), increasing the CR confinement and reducing the acceleration time. Additional increase in the acceleration efficiency can take place if the magnetic field in the wind is amplified ahead of the shock, for instance due to the vorticity generated by the interaction between the CR pressure and density fluctuations in the supersonic wind (Beresnyak et al. 2009; del Valle et al. 2016).

If the non-thermal emission scenario discussed here is indeed correct, future simultaneous broadband outbursts (if detected) will further constrain the properties of the claimed SMBH binary in OJ 287. Also, the data of future outbursts may be applied to test shock acceleration models as well as more realistic multidimensional models of AGN-winds and coronae.

⁴ OJ 287 is in declination favourable for detection with Ice-Cube and estimated as a potential source of HE neutrinos based on a different emission scenario than the one discussed here (Oikonomou et al. 2019).

ACKNOWLEDGEMENTS

We are thankful to the anonymous reviewer for providing valuable critics which improved the quality of this work. We acknowledge support from the Brazilian agencies FAPESP (JCRR's grant: 2017/12188-5, PK's grant: 2015/13933-0, and EMGDP's grant: 2013/10559-5), CNPq (EMGDP's grant: 306598/2009-4), and PK's ARIES Aryabhata Fellowship (AO/A-PDF/770).

DATA AVAILABILITY

The datasets employed in this research were derived in the papers by Kushwaha et al. (2013), and Kushwaha et al. (2018b) from sources in the public domain: High Energy Astrophysics Science Archive Research Centre (HEASARC; <https://fermi.gsfc.nasa.gov/ssc/>) maintained by the National Aeronautics and Space Administration (NASA), SMARTS Optical/IR Observations of Fermi Blazars (<http://www.astro.yale.edu/smarts/glast/home.php>), and Steward Observatory spectropolarimetric monitoring project (<http://james.as.arizona.edu/~psmith/Fermi/>). The data underlying this article will be shared on request.

REFERENCES

- Aharonian F. A., Atoyan A. M., 2000, *A&A*, **362**, 937
 Aharonian F. A., Kririllov-Ugrumov V. G., Vardanian V. V., 1985, *Ap&SS*, **115**, 201
 Atoyan A. M., Dermer C. D., 2003, *ApJ*, **586**, 79
 Atwood W. B., et al., 2009, *ApJ*, **697**, 1071
 Begelman M. C., Blandford R. D., Rees M. J., 1980, *Nature*, **287**, 307
 Beresnyak A., Jones T. W., Lazarian A., 2009, *ApJ*, **707**, 1541
 Blumenthal G. R., Gould R. J., 1970, *Reviews of Modern Physics*, **42**, 237
 Britzen S., et al., 2018, *MNRAS*, **478**, 3199
 Burrows D. N., et al., 2005, *Space Sci. Rev.*, **120**, 165
 Capellupo D. M., Hamann F., Shields J. C., Halpern J. P., Barlow T. A., 2013, *MNRAS*, **429**, 1872
 Caprioli D., Spitkovsky A., 2014, *ApJ*, **783**, 91
 Celli S., Morlino G., Gabici S., Aharonian F. A., 2019, *MNRAS*, **490**, 4317
 Deane R. P., et al., 2014, *Nature*, **511**, 57
 Dey L., et al., 2018, *ApJ*, **866**, 11
 Dey L., et al., 2019, *Universe*, **5**, 108
 Edgar R., 2004, *New Astron. Rev.*, **48**, 843
 Fabian A. C., Lohfink A., Kara E., Parker M. L., Vasudevan R., Reynolds C. S., 2015, *MNRAS*, **451**, 4375
 Ferguson J. W., Alexander D. R., Allard F., Barman T., Bodnarik J. G., Hauschildt P. H., Hefner-Wong A., Tamanai A., 2005, *ApJ*, **623**, 585
 Finke J. D., Razzaque S., Dermer C. D., 2010, *ApJ*, **712**, 238
 Giacalone J., Jokipii J. R., 2007, *ApJ*, **663**, L41
 Ginzburg V. L., Syrovatskii S. I., 1964, *The Origin of Cosmic Rays*. Macmillan
 Giustini M., Proga D., 2019, *A&A*, **630**, A94
 Gupta A. C., et al., 2017, *MNRAS*, **465**, 4423
 Gupta A. C., et al., 2019, *AJ*, **157**, 95
 Hodgson J. A., et al., 2017, *A&A*, **597**, A80
 Hoyle F., Lyttleton R. A., 1939, *Proceedings of the Cambridge Philosophical Society*, **35**, 405

- Hudec R., Bašta M., Pihajoki P., Valtonen M., 2013, *A&A*, **559**, A20
- Iglesias C. A., Rogers F. J., 1996, *ApJ*, **464**, 943
- Irwin J. A., 2007, *Astrophysics: Decoding the Cosmos*. Wiley-VCH Verlag
- Ivanov P. B., Igumenshchev I. V., Novikov I. D., 1998, *ApJ*, **507**, 131
- Kadowaki L. H. S., de Gouveia Dal Pino E. M., Singh C. B., 2015, *ApJ*, **802**, 113
- Katz J. I., 1997, *ApJ*, **478**, 527
- Kelner S. R., Aharonian F. A., Bugayov V. V., 2006, *Phys. Rev. D*, **74**, 034018
- Kieffer T. F., Bogdanović T., 2016, *ApJ*, **823**, 155
- Komossa S., Zensus J. A., 2016, in Meiron Y., Li S., Liu F. K., Spurzem R., eds, *IAU Symposium Vol. 312, Star Clusters and Black Holes in Galaxies across Cosmic Time*. pp 13–25 ([arXiv:1502.05720](https://arxiv.org/abs/1502.05720), doi:10.1017/S1743921315007395)
- Kushwaha P., 2020, *Galaxies*, **8**, 15
- Kushwaha P., Sahayanathan S., Singh K. P., 2013, *MNRAS*, **433**, 2380
- Kushwaha P., de Gouveia Dal Pino E. M., Gupta A. C., Wiita P. J., 2018a, in *International Conference on Black Holes as Cosmic Batteries: UHECRs and Multimessenger Astronomy*. 12-15 September 2018. Foz do Iguacu. p. 22
- Kushwaha P., et al., 2018b, *MNRAS*, **473**, 1145
- Kushwaha P., et al., 2018c, *MNRAS*, **479**, 1672
- Lehto H. J., Valtonen M. J., 1996, *ApJ*, **460**, 207
- Liu B. F., Taam R. E., Qiao E., Yuan W., 2017, *ApJ*, **847**, 96
- Longair M. S., 2011, *High Energy Astrophysics*. Cambridge University Press
- Mannheim K., Schlickeiser R., 1994, *A&A*, **286**, 983
- Melioli C., de Gouveia Dal Pino E. M., 2015, *ApJ*, **812**, 90
- Mingarelli C. M. F., et al., 2017, *Nature Astronomy*, **1**, 886
- Mizuno Y., Pohl M., Niemiec J., Zhang B., Nishikawa K.-I., Hardee P. E., 2014, *MNRAS*, **439**, 3490
- Nayakshin S., Cuadra J., Sunyaev R., 2004, *A&A*, **413**, 173
- Neronov A., Vovk I., 2011, *MNRAS*, **412**, 1389
- Oikonomou F., Murase K., Padovani P., Resconi E., Mészáros P., 2019, *MNRAS*, **489**, 4347
- Pai S.-I., Luo S., 1991, *Theoretical and Computational Dynamics of a Compressible Flow*. Springer Science+Business Media New York
- Pal M., Kushwaha P., Dewangan G. C., Pawar P. K., 2020, *ApJ*, **890**, 47
- Petropoulou M., Kamble A., Sironi L., 2016, *MNRAS*, **460**, 44
- Pfeifle R. W., et al., 2019, *ApJ*, **883**, 167
- Pihajoki P., 2016, *MNRAS*, **457**, 1145
- Popović L. Č., 2012, *New Astron. Rev.*, **56**, 74
- Ptuskin V. S., Moskalenko I. V., Jones F. C., Strong A. W., Zirakashvili V. N., 2006, *ApJ*, **642**, 902
- Romero G. E., Vieyro F. L., Vila G. S., 2010, *A&A*, **519**, A109
- Shibata S., Tominaga N., Tanaka M., 2014, *ApJ*, **787**, L4
- Sillanpaa A., Haarala S., Valtonen M. J., Sundelius B., Byrd G. G., 1988, *ApJ*, **325**, 628
- Slone O., Netzer H., 2012, *MNRAS*, **426**, 656
- Springel V., et al., 2005, *Nature*, **435**, 629
- Sturmer S. J., Skibo J. G., Dermer C. D., Mattox J. R., 1997, *ApJ*, **490**, 619
- Tanaka T. L., 2013, *MNRAS*, **434**, 2275
- Valtonen M. J., et al., 2008, *Nature*, **452**, 851
- Valtonen M. J., et al., 2016, *ApJ*, **819**, L37
- Valtonen M. J., et al., 2019, *ApJ*, **882**, 88
- Verigin M., et al., 2003, *Journal of Geophysical Research (Space Physics)*, **108**, 1323
- Zanotti O., Roedig C., Rezzolla L., Del Zanna L., 2011, *MNRAS*, **417**, 2899
- Zentsova A. S., 1983, *Ap&SS*, **95**, 11
- del Valle M. V., Lazarian A., Santos-Lima R., 2016, *MNRAS*, **458**, 1645

APPENDIX A: THE ENERGY STORED BY THE BH-DISC COLLISION

Here we estimate the energy injected by the secondary BH after its passage through the disc of the primary one. To do this, we assume that Bondi-Hoyle-Lyttleton (BHL) accretion theory (Hoyle & Lyttleton 1939; Edgar 2004; Zanotti et al. 2011) describes well the accretion of the disc material onto the travelling BH. As noted by Ivanov et al. (1998) and Pihajoki (2016), this turns out to be the case if the thickness ΔH of the accretion disc is $\Delta H \gg R_{\text{HL}}$ at the location of the impact, where R_{HL} the Bondi-Hoyle-Lyttleton radius of the travelling BH:

$$R_{\text{HL}} = \frac{2GM_2}{v_r^2}, \quad (\text{A1})$$

and v_r the resultant velocity of the disc material in the co-moving frame of the travelling BH (see Figure A1, upper). Thus, the estimate described in the following, is more reliable the smaller the ratio $R_{\text{HL}}/\Delta H$.

A wake of shocked material is formed behind the travelling BH provided that its velocity is supersonic with respect to the sound speed of the disc fluid, which is the case for the situation discussed here. In the co-moving frame of the secondary BH, the upstream flow impinging at cylindrical radii $\leq R_{\text{HL}}$ is eventually accreted onto the gravitational source (see Figure A1, lower panel). On the other hand, there is an amount of upstream gas impinging at cylindrical radii $> R_{\text{HL}}$ that is deflected by the BH gravity, is compressed through the shock (downstream), and have enough kinetic energy to not fall onto the BH as illustrated in Figure A1 (lower panel).

We consider $\Delta t = \Delta H/v_{\text{orb}}$ as the time scale of the impact event, where v_{orb} is the velocity of the secondary BH at the location of the impact. Additionally, we consider that the kinetic energy of the upstream flow impinging at cylindrical radii between R_{HL} and $(1 + \delta)R_{\text{HL}}$ (where δ is a control dimensionless parameter) during the time interval Δt will eventually drive the outflows that emerge from the disc. Due to the gravity of the secondary BH, the material flowing upstream through the annulus defined by the radii R_{HL} and $(1 + \delta)R_{\text{HL}}$ converges downstream of the BH (as illustrated in Figure A1, lower panel). Motivated by the numerical simulations of Ivanov et al. (1998), here we assume that this converging material eventually split in two outflows that emerge above and below the accretion disc. The morphology of the emerging outflows may be initially highly asymmetric. Nevertheless, to proceed analytically we consider the emerging outflows as expanding spheres with physical properties (such as temperature, gas density, and radius) equivalent to the average properties of the “real” outflows.

The kinetic energy of the upstream flow impinging between R_{HL} and $(1 + \delta)R_{\text{HL}}$ can be estimated as

$$E_K = A\Delta t \frac{dE}{dAdt}, \quad (\text{A2})$$

where $A = \pi(2\delta + \delta^2)R_{\text{HL}}^2$ and $\frac{dE}{dt dA} = \frac{1}{2}\rho_d v_r^3$ is the flux of (the upstream) kinetic energy. Thus, assuming conservation

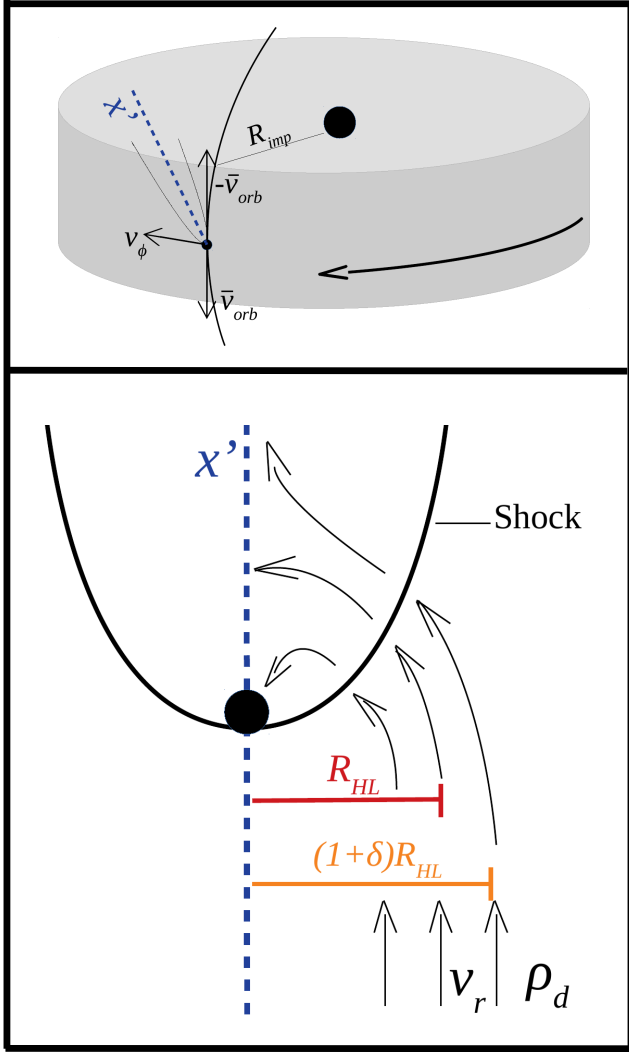


Figure A1. Upper: Schematic illustration of Bondi-Hoyle-Lyttleton accretion onto the secondary BH (the small black circle) while traversing the accretion disc of the primary (the big black circle, see the text). The grey cylinder represents the central volume of the accretion disc within the radius R_{imp} (the radius at which the secondary BH impacts the disc). The arrows represent the velocity of the travelling BH (\vec{v}_{orb}) and the toroidal component of accretion disc fluid velocity (\vec{v}_{ϕ}). Lower: Schematic view in the co-moving frame of the travelling BH. In this frame the disc material of density ρ_d impinges the secondary BH with velocity $v_r = |\vec{v}_{\phi} - \vec{v}_{\text{orb}}|$. The red bar represents the Bondi-Hoyle-Lyttleton radius R_{HL} (see equation 2). Particularly, the material impinging at radii between R_{HL} and $(1 + \delta)R_{\text{HL}}$ is not accreted onto the travelling BH.

of energy and that the energy given by equation (A2) equally split among the two outflows that emerge, the energy E_0 of each outflow is:

$$E_0 = \frac{\pi}{4} (2\delta + \delta^2) \left(\frac{\Delta H}{R_{\text{HL}}} \right) \left(\frac{v_r}{v_{\text{orb}}} \right) R_{\text{HL}}^3 \rho_d v_r^2, \quad (\text{A3})$$

Similarly, assuming conservation of mass, the mass M_0 of each outflow is

$$M_0 = \frac{\pi}{2} (2\delta + \delta^2) \left(\frac{\Delta H}{R_{\text{HL}}} \right) \left(\frac{v_r}{v_{\text{orb}}} \right) R_{\text{HL}}^3 \rho_d. \quad (\text{A4})$$

As described in the main text of this paper, we parametrise the outflows as spherical blobs that emerge the disc with initial radius $R_0 = f_R R_{\text{HL}}$, ($f_R \leq 1$) and initial gas density $\rho_0 = 7\rho_d$ (given by the compression of a strong, radiation dominated shock). In terms of this parametrisation, the mass of the each blob can be expressed as

$$M_0 = \frac{4\pi}{3} (f_R R_{\text{HL}})^3 7\rho_d. \quad (\text{A5})$$

Combining equations (A4)-(A5), the dimensionless control parameter δ is given by

$$(2\delta + \delta^2) \left(\frac{\Delta H}{R_{\text{HL}}} \right) \left(\frac{v_r}{v_{\text{orb}}} \right) = \frac{56}{3} f_R^3, \quad (\text{A6})$$

and combining (A6) with equation (A3), the energy of each blob can be expressed as

$$E_0 = \frac{14\pi}{3} (f_R R_{\text{HL}})^3 \rho_d v_r^2. \quad (\text{A7})$$

APPENDIX B: ENERGY LOSSES OF CR PROTONS

The rate of energy losses due to diffusion of CR protons in equation (34) is calculated as

$$t_{\text{diff}}^{-1} = 2D(E_p, B)/R_b^2, \quad (\text{B1})$$

where D is the diffusion coefficient defined in equation (32) and R_b is the radius of the outflow bubble.

The rate of energy losses due to proton-proton interactions is computed as:

$$t_{\text{pp}}^{-1}(E_p, n_0) = K_{\text{pp}} c n_0 \sigma_{\text{pp}}(E_p), \quad (\text{B2})$$

where $K_{\text{pp}} \sim 0.5$ is the inelasticity factor, σ_{pp} is the total cross section for p - p interactions taken from Kelner et al. (2006), and n_0 is the local density of thermal ions. We employ equation (B2) to calculate the rate of proton-proton interactions in the region within the outflow bubble as well as in the shell of the shocked AGN wind material. For the region within the outflow bubble we set $n_0 = n_b$ (the density of the bubble, see equation 7). Distinctly from the gas of the bubble, the gas in the shell of shocked AGN wind is not radiation pressure dominated (see equation 26 and related text). Thus, in the swept up shell we set $n_0 = 4n_w$, where n_w is the gas number density of the impinging AGN wind. This corresponds to the case of a strong shock and the specific heat ratio of $\gamma_{\text{sh}} = 5/3$.

The rate of energy losses of protons due to photo-pion production is computed as (e.g., Atoyan & Dermer 2003; Romero et al. 2010):

$$t_{\text{p}\gamma}^{-1}(E_p) = \frac{m_p^2 c^5}{2E_p^2} \int_{\frac{\epsilon_{\text{th}}}{2\gamma_p}}^{\infty} d\epsilon \frac{n_{\text{ph}}(\epsilon)}{\epsilon^2} \int_{\epsilon_{\text{th}}}^{2\epsilon\gamma_p} d\epsilon' \epsilon' K_{\text{p}\gamma}(\epsilon') \sigma_{\text{p}\gamma}(\epsilon'), \quad (\text{B3})$$

where, $\epsilon_{\text{th}} = 145$ MeV is the photon energy threshold for pion production in the rest-frame of the incident proton. For the inelasticity and the total cross section of the interaction, $K_{\text{p}\gamma}$ and $\sigma_{\text{p}\gamma}$, we follow the approximation given by Atoyan & Dermer (2003).

APPENDIX C: ELECTRON ENERGY LOSSES

According to equation (45), we calculate the energy distribution of secondary e^\pm pairs by considering the energy losses of this particle population due to synchrotron radiation P_{syn} , inverse Compton scattering P_{IC} , relativistic bremsstrahlung P_{br} , and Coulomb collisions P_{Co} .

We calculate the energy losses due to synchrotron cooling as:

$$P_{\text{syn}} = \frac{4}{3} \sigma_{\text{T}} c \frac{B^2}{8\pi} \left(\frac{E_e}{m_e c^2} \right)^2, \quad (\text{C1})$$

with $\sigma_{\text{T}} = 6.652 \text{ cm}^2$ the Thomson cross section, m_e the electron rest mass and B the local magnetic field density.

The IC seed photon field considered here (the thermal bremsstrahlung radiation from the outflow bubble; see Section 2.1) has cut-off at $\sim 1 \text{ eV}$. Thus for secondary electrons with energy $\lesssim 10^{11} \text{ eV}$, the IC scattering occurs in the Thompson regime, and their IC energy losses rate is given by:

$$P_{\text{IC}} = \frac{4}{3} \sigma_{\text{T}} c U_{\text{ph}} \left(\frac{E_e}{m_e c^2} \right)^2, \quad (\text{C2})$$

where

$$U_{\text{ph}} = \int_{\epsilon_{\text{min}}}^{\epsilon_{\text{max}}} \epsilon n_{\text{ph}}(\epsilon) d\epsilon, \quad (\text{C3})$$

is the energy density of the photon field in the emission region of the e^\pm pairs, and $n_{\text{ph}}(\epsilon)$ is the photon field density generated by the thermal bremsstrahlung radiation of the outflow bubble (see equation 18).

Assuming a fully ionised medium, the cooling of e^\pm by relativistic bremsstrahlung is calculated as (e.g., [Sturmer et al. 1997](#)):

$$P_{\text{br}} = \frac{8e^6 n_{\text{b}}}{\hbar m_e c^2} (\ln \{\gamma_e\} + 0.36) (\gamma_e + 1), \quad (\text{C4})$$

with $\gamma_e = E_e/(m_e c^2)$.

The energy loss rate due to Coulomb collisions of CR electrons with background thermal electrons is calculated as (e.g., [Mannheim & Schlickeiser 1994](#); [Sturmer et al. 1997](#)):

$$P_{\text{Co}} = \frac{2\pi e^4}{m_e c} \frac{n_{\text{b}} \lambda_{\text{Co}}}{\beta_e} [\psi(x) - \psi'(x)], \quad (\text{C5})$$

where $\lambda_{\text{Co}} \sim 15$ is the Coulomb logarithm for the parameters of the problem of this work, $\beta_e = v_e/c = \sqrt{1 - 1/\gamma_e^2}$ is the velocity of CR electrons in units of the speed of light, and

$$\psi(x) = \frac{2}{\sqrt{\pi}} \int_0^x y^{1/2} \exp\{-y\} dy, \quad (\text{C6})$$

$$\psi'(x) = \frac{d\psi}{dx}, \quad (\text{C7})$$

where $x = m_e v_e^2/(2kT_e)$, being T_e the electron temperature inside the bubble given by equation (6).

This paper has been typeset from a $\text{\TeX}/\text{\LaTeX}$ file prepared by the author.